Publications of the Astronomical Society of Japan, 2025, **77**(SP1), S50–S62
https://doi.org/10.1093/pasj/psaf045
Advance access publication date: 2025 June 3

Spectroscopic diagnostics of high-temperature plasma in stellar coronae using Fe XXIV–XXIV K-shell lines with XRISM

Miki KURIHARA,[1,2,*] Masahiro TSUJIMOTO,[2] Marc AUDARD,[3] Ehud BEHAR,[4] Liyi GU,[5] Kenji HAMAGUCHI,[6,7] Natalie HELL,[8] Caroline A. KILBOURNE,[6] Yoshitomo MAEDA,[2] Frederick S. PORTER,[6] Haruka SUGAI,[9] and Yohko TSUBOI[9]

[1]Department of Astronomy, Graduate School of Science, The University of Tokyo, 7-3-1 Hongo, Bunkyo-ku, Tokyo 113-0033, Japan
[2]Japan Aerospace Exploration Agency, Institute of Space and Astronautical Science, 3-1-1 Yoshinodai, Chuo-ku, Sagamihara-shi, Kanagawa 252-5210, Japan
[3]Department of Astronomy, University of Geneva, CH-1290 Versoix, Switzerland
[4]Department of Physics, Technion, Technion City, Haifa 3200003, Israel
[5]SRON Netherlands Institute for Space Research, Niels Bohrweg 4, 2333 CA Leiden, the Netherlands
[6]NASA's Goddard Space Flight Center, Greenbelt, MD 20771, USA
[7]Department of Physics, University of Maryland, Baltimore County, Baltimore, MD 21250, USA
[8]Lawrence Livermore National Laboratory, CA 94550, USA
[9]Department of Physics, Faculty of Science and Engineering, Chuo University, 1-13-27 Kasuga, Bunkyo, Tokyo 112-8551, Japan
*Email: kurihara@ac.jaxa.jp

Abstract

The RS CVn type binary star GT Muscae was observed during its quiescence using the Resolve X-ray microcalorimeter spectrometer onboard XRISM. The main and satellite lines of the Fe XXIV–XXIV K-shell transitions were resolved for the first time from stellar sources. We conducted line ratio analysis to investigate any deviations from collisional ionization equilibrium and Maxwell electron energy distribution with a single temperature. By using five combinations of direct excitation lines and dielectronic recombination satellite lines in three line complexes (Fe Heα, Lyα, and Heβ), we found that the plasma is well characterized by two-temperature thermal plasmas with temperatures of 1.7 and 4.3 keV, which is consistent with thermal broadening of Fe XXV, and the broad-band fitting results in the 1.7–10 keV band. Other forms of deviation from a single-temperature plasma, such as different ionization and electron temperatures or the κ distribution for the electron energy distributions, are not favored, which is reasonable for stellar coronae at quiescence. This study demonstrates the utility of the Fe K-shell line ratio diagnostics to probe plasma conditions using X-ray microcalorimeters.

Keywords: atomic processes — stars: coronae — stars: individual (GT Mus) — techniques: spectroscopic — X-rays: stars

1 Introduction

Collisional plasmas in the Universe often deviate from the thermal equilibrium of a single temperature. The deviation provides insights into the spatial distribution, the dynamics, and the mechanism of heating of such plasmas through the equilibration processes. The deviation can take several different forms, including the multi-temperature distribution, the suprathermal electron energy distribution, and non-equilibrium ionization (NEI). The multi-temperature distributions are often seen in systems of different plasma sources integrated in the line of sight. Suprathermal electrons represented by an additional higher-energy population upon the thermal Maxwellian distribution are also seen in in situ observations of heliospheric plasmas (e.g., Maksimovic et al. 1997). NEI plasmas occur when ions are either underionized or overionized relative to the electron temperature, which is a feature ubiquitously seen in tenuous plasmas of an impulsive energy injection such as supernova remnants (e.g., Vink 2020; Yamaguchi & Ohshiro 2022).

X-ray line ratio measurements are a promising method for probing these departures from thermal equilibrium. Deviated conditions influence the ionization, recombination, and excitation rates, which in turn affect the charge and level populations, thereby modifying the intensity of emission lines. For multi-temperature and suprathermal plasma diagnostics, Gabriel (1972) and Gabriel and Phillips (1979) first proposed using lines formed by the dielectronic recombination (DR) process, which are sensitive to variations in electron energy distributions. For NEI diagnostics, the ratio of strong direct excitation (DE) lines from ions of different charge states is useful.

The Fe K-shell line complex at 6–9 keV provides particularly rich information for several reasons. Fe has the largest atomic number (Z) among abundant elements in the Universe. The K-shell line energies increase with Z and those of Fe probe the plasma of temperatures at 1–10 keV (see Hell et al. 2020 for a review). The DR to DE line ratio scales roughly as Z^4 (Gabriel & Paget 1972); thus the weaker DR lines are more accessible as Z increases. The ionization parameter $\tau = \int dt\, n_e$, where n_e is electron density, is a measure of the Coulomb relaxation timescale of NEI plasmas. Its Z dependence was investigated for major elements from C to Ni (Smith & Hughes 2010). In the 1–10 keV temperature range, the time to reach an equilibrium is longer for higher-Z

Received: 2025 March 9; **Accepted:** 2025 April 9

elements than lower-Z elements, which were studied using the X-ray grating spectrometers onboard Chandra and XMM–Newton (e.g., Audard 2003; Nordon & Behar 2007).

In order to take advantage of the Fe K-shell lines, a spectral resolving power $R \equiv E/\Delta E \gtrsim 1000$ is required for the energy band $E \gtrsim 6.4$ keV. Until the advent of the X-ray microcalorimeter spectrometers, this was achieved only in some selected narrow energy bands for solar X-ray observations using rotating or bent crystal spectrometers onboard P78-1, Hinotori (Astro-A), Yohkoh (Solar-A), and SMM (Doschek et al. 1979, 1980; Feldman et al. 1980; Dubau et al. 1981; Parmar et al. 1981; Tanaka et al. 1982; Tanaka 1986; Watanabe 2024), The first X-ray microcalorimeter observation was made using the Soft X-ray Spectrometer (SXS: Kelley et al. 2016) onboard Hitomi (Astro-H: Takahashi et al. 2018) for the Perseus cluster of galaxies (Hitomi Collaboration 2018a). Despite its short lifetime, the SXS demonstrated the capability of X-ray microcalorimeters for diagnosing celestial plasmas using Fe K-shell lines over a wide energy range covering higher series ($n \rightarrow 1$; $n \geq 2$) lines (Hitomi Collaboration 2018b).

The unique capability of the SXS is now recovered with the Resolve instrument (Ishisaki et al. 2022) onboard the X-ray Imaging and Spectroscopy Mission (XRISM; Tashiro et al. 2020). The instrument has been yielding high-resolution Fe K-shell spectra of collisionally ionized plasmas from interstellar gas (XRISM Collaboration 2025c), supernova remnants (XRISM Collaboration 2024), and clusters of galaxies (XRISM Collaboration 2025a; 2025b). Stars are an important category for applying plasma diagnostics for their relatively slow bulk and turbulent motions, which make interpretation easier, as well as their rapid dynamical developments on human timescales during flares. Comparison to the Sun (e.g., Huenemoerder et al. 2013) is also unique to stellar sources.

In this paper, we present the first results of the Fe K-shell line diagnostics of stellar coronae using an X-ray microcalorimeter. Line ratio analysis is performed to investigate any deviations from single-temperature plasmas. In addition to modeling the Fe Heα and Lyα complexes as in solar studies, we also use the Fe Heβ complex at 7.781 keV, which was observed with $R > 1000$ for the first time in stars including the Sun (Phillips et al. 2012).

The outline of this paper is as follows. In section 2, we describe the target, XRISM observation, and data reduction. In section 3, we present the Resolve light curve and X-ray spectrum, followed by the results of the spectral fitting analysis. In section 4, we apply the line ratio techniques and discuss the plasma properties. In section 5, we summarize the findings and provide the conclusion. Throughout the paper, the quoted uncertainties are for 90% statistical error.

2 Observations

2.1 Target

GT Muscae (GT Mus) is the target of this study. It is a quadruple system at a distance of ∼141 pc by a parallax measurement with Gaia (Gaia Collaboration 2016, 2023). It consists of two binaries: HD 101379 and HD 101380. HD 101379 is a single-line spectroscopic binary composed of a G5 and a G8 giant, while HD 101380 is an eclipsing double-line spectroscopic binary composed of an A0 and an A2 dwarf. The orbital periods of HD 101379 and HD 101380 are 61.4 and 2.7546 d, respectively (Collier et al. 1982; Murdoch et al. 1995). The former is an RS-CVn type source and is considered to be the primary source of X-ray emission.

GT Mus is known to exhibit giant flares, some of which were captured in X-ray observations. The gas proportional counter (GSC: Mihara et al. 2011) onboard the Monitor of All-sky X-ray Image (MAXI: Matsuoka et al. 2009) detected 11 flares in eight years with a peak flux of 34–130 mCrab; the released energy in a single flare amounts to $\sim 10^7$ times that of X-class flares of the Sun (Tsuboi et al. 2016; Sasaki et al. 2021). The highest-energy photons were detected from GT Mus among all stellar flares using the INTEGRAL (Winkler et al. 2003) soft gamma-ray imager (ISGRI; Lebrun et al. 2003) at up to 40 keV during a flare (Sguera et al. 2016). Such giant flares are rare, and their peaks are difficult to capture by X-ray telescopes with a small field of view.

The X-ray Imaging Spectrometer (XIS: Koyama et al. 2007) onboard Suzaku (Astro-E2: Mitsuda et al. 2007) and the Neutron star Interior Composition ExploreR (NICER: Gendreau et al. 2016) observed the decaying phase of flares (Xu et al. 2016; Sasaki et al. 2021; Eze et al. 2022) and recorded thermal plasma emission with a temperature of ∼5 keV. Some flares last sufficiently long, up to a few days, to fall within the XRISM target-of-opportunity response time. These flares are expected to yield count rates in the appropriate dynamic range of the Resolve X-ray microcalorimeter. Although no such observations have been made at the time of writing, we anticipate a few during the mission.

Even during the quiescent phase, GT Mus is an attractive target. While other stars exhibit soft X-ray emission at a temperature of $\lesssim$2 keV from their stellar coronae (e.g., Sanz-Forcada et al. 2002; Audard et al. 2003; Pandey & Singh 2012), GT Mus exhibits an exceptionally hard X-ray emission with a ∼5 keV temperature even without giant flares (Xu et al. 2016; Sasaki et al. 2021). The cause of its exceptional behavior is not well understood, but it provides a unique opportunity for the Fe K-band spectroscopy of stellar coronae using an X-ray microcalorimeter unconstrained by unpredictable flare behaviors. This is what we present in this paper.

2.2 Instrument

XRISM hosts two scientific instruments that operate simultaneously. One is the X-ray microcalorimeter spectrometer, Resolve (Ishisaki et al. 2022), and the other is the X-ray CCD imaging spectrometer, Xtend (Mori et al. 2022; Noda et al. 2025). In this paper, we focus on the former.

Resolve is an X-ray spectrometer based on X-ray microcalorimetry (McCammon et al. 1984). The detector array consists of 6 × 6 pixels, with each pixel containing a HgTe X-ray absorber and an ion-doped Si thermister thermally anchored to the 50 mK stage (Kilbourne et al. 2018a) controlled by the adiabatic demagnetization refrigerator (ADR: Shirron et al. 2018). One of the 36 pixels is displaced from the array for calibration purposes. The in-orbit performance of energy resolution and absolute energy scale has been evaluated to be $\Delta E \sim 4.5$ eV (FWHM) and $\delta E \sim 0.3$ eV in the Fe K band (Porter et al. 2024; Eckart et al. 2024). The exception is the bandpass; the lower-energy range is currently limited to above 1.7 keV due to the cryostat transmissive window (Midooka et al. 2021), which is yet to be opened.

For the purpose of this study, several unique characteristics of Resolve provide distinct advantages. One is the energy resolution $R = 1300$ at 6 keV, better at higher energies, which

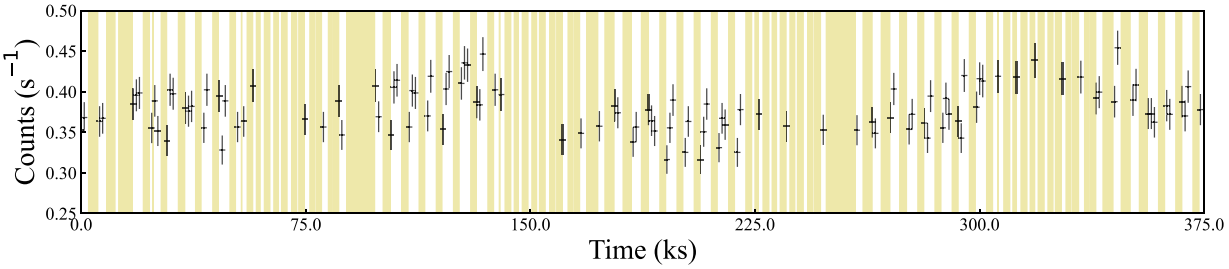

Fig. 1. Resolve light curve at 1.7–10.0 keV with 1024 s binning (bottom) after the standard screening. The time origin is 2024-08-13T02:12:12. The observation intervals are shown with a white background.

enables the separation of fine-structure levels and satellite lines of Fe xxv Heα ($\sim$6.7 keV) and Fe xxiv Lyα (7.0 keV) line complexes. Another advantage is the high-energy end of the bandpass, which is achieved by the HgTe absorbers instead of the Si absorbers in conventional X-ray spectrometers. Together with a high throughput and low background rate, this allows the detection of higher-series lines such as Fe xxv Heβ at 7.8 keV. X-ray spectrometers with such unique features have not been achieved even in solar observations.

2.3 Observation and data reduction

GT Mus was observed as one of the performance verification phase targets (sequence number 300000010) from 2024 August 13 02:03:40 to August 17 10:12:28 (UT). The total telescope time of 375 ks was interrupted by (i) occultation of the target by the Earth, (ii) XRISM passages through the South Atlantic Anomaly (SAA) region, (iii) ADR recycling, and (iv) ^{55}Fe source illumination for calibration. As a result, the observing efficiency was 53%, yielding an effective exposure time of 199 ks (figure 1).

The Resolve energy scale was calibrated both on the ground and using on-board calibration sources in flight (Eckart et al. 2024). The time-dependent detector gain directly affects the energy scale and was corrected during the observation of GT Mus using periodic observations of ^{55}Fe X-ray sources installed on the instrument filter wheel (FW) assembly. The sources were rotated into the field of view (FOV) during several Earth occultations of the celestial target. For this observation, there were 12 observations of $\sim$30 min of the FW sources that were then used to correct the time-dependent detector gain in the standard process for Resolve (Porter et al. 2016, 2024). Resolve also contains a calibration pixel that is located on the main detector array but just outside of the FOV. The calibration pixel is used to monitor the efficacy of the gain correction during each observation, outside of the fiducial measurements, since it is illuminated continuously by a dedicated ^{55}Fe X-ray source. For this observation, the energy scale reconstruction was very precise, with the calibration pixel yielding an accuracy of -0.228 ± 0.006 eV at 5.9 keV. This is added in quadrature to the systematic energy scale uncertainties of 0.3 eV from the in-flight calibration to yield an energy scale uncertainty in the region from 5.4–8 keV that is covered by the on-board calibration sources. This yields an estimated uncertainty for this observation of 0.38 eV, 5.4–8 keV. The estimated systematic energy scale uncertainty is $\sim$1 eV from the bottom of the band to 5.4 keV, and $\sim$2 eV above 8 keV. We used the standard Resolve redistribution response matrix file (RMF) generator for this observation that includes the energy-dependent core line spread function (energy resolution) that varies by pixel. The line spread function for Resolve has been verified in flight, and also using the FW fiducial calibrations during this observation. The standard systematic uncertainty in the core line spread function for Resolve is 0.13 eV at 6 keV and 0.17 eV at 7 keV.

We started with the products of the standard pipeline version 03.00.011.008 (Doyle et al. 2022). We combined all 35 pixels in the array and used high-primary (Hp) grade events only, which are temporally isolated from other events in the same pixel and are well calibrated for high-resolution spectroscopy. We applied further screening to reduce background events based on X-ray pulse rise time and energy (Mochizuki et al. 2025). The fraction of the Hp grade events is 0.96, and the resultant mean count rate is 0.38 s^{-1} in the 1.7–12 keV band. This count rate is low enough to disregard artifacts caused by high count rates (Mizumoto et al. 2025). The background rate is also negligible in the energy range of interest (Kilbourne et al. 2018b).

We used `HEASoft` version 6.34.0 for data analysis. The spectrum was optimally binned (Kaastra & Bleeker 2016), with a minimum of 10 counts per bin. The telescope and detector response files were generated using the `xaarfgen` and `rslmkrmf` tasks, respectively. For the detector response, we included off-diagonal components in the redistribution matrix to account for escape peaks, Si fluorescence, and electron loss continuum, in addition to the diagonal line spread function at the core. For the background, we used a model spectrum of the non-X-ray background[1] and adjusted its normalization with a diagonal response to match the observed spectrum in the 14–17 keV range, where celestial counts are negligible.

3 Analysis

We present the X-ray light curve and spectrum in subsection 3.1, and describe the entire spectrum with a single-temperature plasma model (sub-subsection 3.2.1) and individual line complexes with phenomenological models (sub-subsection 3.2.2).

3.1 Light curve and spectrum

Figure 1 shows the 1.7–10 keV light curve. The X-ray flux is consistent with previous observation of GT Mus during

[1] ⟨https://heasarc.gsfc.nasa.gov/docs/xrism/analysis/nxb/nxb_spectral_models.html⟩.

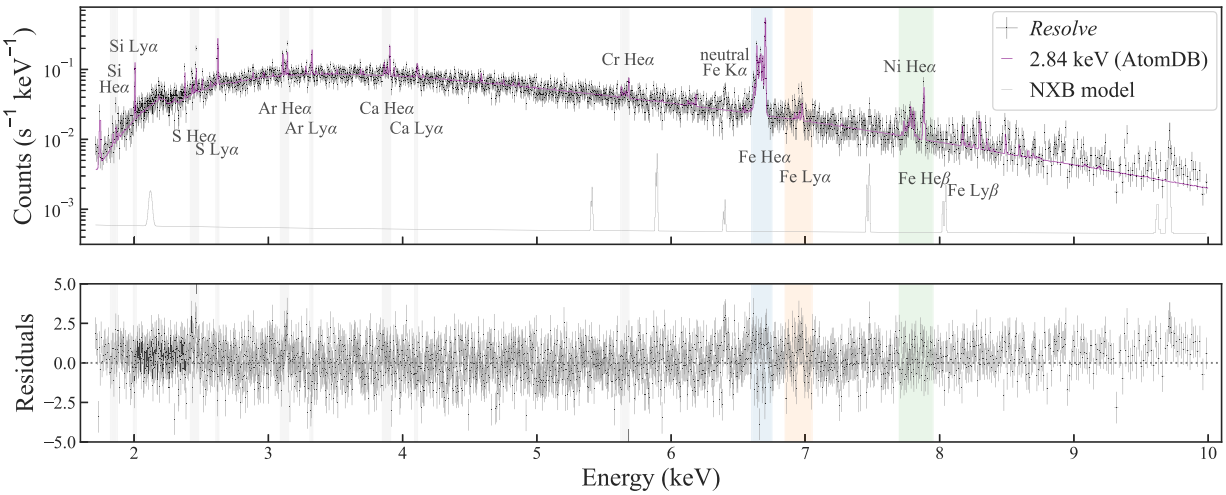

Fig. 2. (top) Resolve spectrum at 1.7–10.0 keV with optimal binning (black crosses) compared to the fiducial 2.84 keV thermal plasma model (purple curve) and the background model spectrum (gray). The blue, orange, and green stripes indicate the Fe Heα, Lyα, and Heβ line complexes, which we study in more detail in figure 3. (bottom) The residuals to the fiducial model fit.

quiescence (Sasaki et al. 2021). Given the small variability and the observation duration being much shorter than the orbital period of the RS CVn binary (∼61.4 d), we combined all events into a single spectrum without time slicing.

Figure 2 shows the 1.7–10 keV spectrum. Numerous lines are recognized upon the continuum, including the Heα and Lyα lines of Si, S, Ar, Ca, Cr, Mn, Fe, and Ni, as well as the Heβ and Lyβ lines of Fe. The Kα fluorescence lines of quasi-neutral Fe are also found. Notably, Fe K features are particularly prominent, with the line complexes of Fe xxv Heα, Fe xxiv Lyα, and Fe xxv Heβ clearly resolved. A comparison with the background spectrum confirms that its contamination is negligible except for Au L lines at 9.7 keV.

3.2 Spectral modeling

3.2.1 Broad-band

We first constructed the fiducial model for the broad-band spectrum using the 1.7–10 keV band source spectrum. The background spectrum was not subtracted, as its contribution is negligible with $\lesssim$10%. Spectral fitting was performed using the `xspec` software based on χ^2 statistics (Arnaud 1996).

The model consists of a single-temperature thermal plasma emission (`apec` model; Smith et al. 2001) attenuated by the X-ray photoelectric absorption by the interstellar matter (Wilms et al. 2000). The chemical abundance table of Anders and Grevesse (1989) was used. The best-fitting values of free parameters are the plasma temperature ($kT = 2.84^{+0.04}_{-0.03}$ keV) and the volume emission measure ($EM = 31.4^{+0.5}_{-0.5} \times 10^{54}$ cm^{-3}); the relative abundances of Fe ($Z_{\rm Fe} = 0.25^{+0.01}_{-0.01}\ Z_\odot$), Ni ($Z_{\rm Ni} = 0.41^{+0.16}_{-0.15}\ Z_\odot$), and the other major elements (0.36–0.7 $Z_\odot$); and the interstellar absorption column density ($N_{\rm H} = 1.0 \times 10^{14}\ ^{+8.2\times10^{21}}_{-1.0\times10^{14}}$ cm^{-2}). A satisfactory result was obtained with a reduced $\chi^2 = 2429.56/2169$, which describes the overall spectrum well (figure 2), although some residuals remain in the Fe K complexes. In the broad-band fitting using the χ^2 statistics, informative line features are not fully utilized, as spectral bins with continuum emission dominate the statistics. We further examine these line complexes using a different approach below.

3.2.2 Line complexes

We describe the line complexes using a phenomenological model consisting of individual emission lines and a continuum. Three energy bands, colored in figure 2, are fitted separately: Fe xxv Heα (blue; 6.603–6.750 keV), Fe xxiv Lyα (orange; 6.850–7.050 keV), and Fe xxv Heβ (green; 7.700–7.950 keV). The lines used for the phenomenological fittings are summarized in table 1.

3.2.2.1 Models

The model for the Fe Heα complex was constructed as follows. It is composed of main lines of Fe xxv and satellite lines of Fe xxiii–xxiv. We selected the 16 strongest lines based on the `Chianti` code (Dere et al. 1997, 2023) for the 2.84 keV thermal plasma (sub-subsection 3.2.1). We confirmed that the dependence on the electron density ($n_{\rm e}$) is negligible for $n_{\rm e} \leq 10^{14}$ cm^{-3}. The number of selected lines was determined considering the blending by non-selected weaker lines and the data statistics, referring to the previous ground measurements (Beiersdorfer et al. 1993; Decaux et al. 1997; Gu et al. 2012) and solar observation (e.g., Watanabe 2024). The continuum emission is represented by the `nlapec` model (Smith et al. 2001) in `xspec`, which is equivalent to the `apec` model for thermal plasma emission but without emission lines having emissivities larger than 10^{-20} cm^3 s^{-1}. Unlike the simple Bremsstrahlung model, `nlapec` also includes contributions by the radiative recombination continuum as well as the weak emission lines.

The model for the Fe Lyα complex was constructed in a similar way. Along with the continuum emission represented by the `nlapec` model, four emission lines are included, representing the two main lines of Fe xxiv Lyα1 and Lyα2 as well as two satellite lines of Fe xxv J and T.

The model for the Heβ complex needs to account for contamination from the overlapping Ni Heα line complex. Instead of using the `nlapec` model, we employed the `apec` model but removed the three Fe lines in the complex, so that

Table 1. Line list for phenomenological fitting.

Label*	Ion	Lower–upper	E (keV)†
E12	Fe XXIII	$1s^2.2s.2p\ ^3P_2$–$1s.2s.2p^2\ ^3D_3$	6.6097
u‡	Fe XXIV	$1s^2.2s\ ^2S_{1/2}$–$1s.2s(^3S).2p\ ^4P_{3/2}$	6.6167
e‡	Fe XXIV	$1s^2.2p\ ^2P_{3/2}$–$1s.2p^2(^3P)\ ^4P_{5/2}$	6.6203
E3 (β)	Fe XXIII	$1s^2.2s^2\ ^1S_0$–$1s.2s^2.2p\ ^1P_1$	6.6288
z	Fe XXV	$1s^2\ ^1S_0$–$1s.2s\ ^3S_1$	6.6366
j	Fe XXIV	$1s^2.2p\ ^2P_{3/2}$–$1s.2p^2(^1D)\ ^2D_{5/2}$	6.6447
r	Fe XXIV	$1s^2.2s\ ^2S_{1/2}$–$1s.2s(^1S).2p\ ^2P_{1/2}$	6.6529
k	Fe XXIV	$1s^2.2p\ ^2P_{1/2}$–$1s.2p^2(^1D)\ ^2D_{3/2}$	6.6547
a	Fe XXIV	$1s^2.2p\ ^2P_{3/2}$–$1s.2p^2(^3P)\ ^2P_{3/2}$	6.6579
q	Fe XXIV	$1s^2.2s\ ^2S_{1/2}$–$1s.2s(^3S).2p\ ^2P_{3/2}$	6.6622
y	Fe XXV	$1s^2\ ^1S_0$–$1s.2p\ ^3P_1$	6.6676
t‡	Fe XXIV	$1s^2.2s\ ^2S_{1/2}$–$1s.2s(^3S).2p\ ^2P_{1/2}$	6.6762
x	Fe XXV	$1s^2\ ^1S_0$–$1s.2p\ ^3P_2$	6.6827
d13	Fe XXIV	$1s^2.3p\ ^2P_{3/2}$–$1s.2p(^1P).3p\ ^2D_{5/2}$	6.6892
d15	Fe XXIV	$1s^2.3p\ ^2P_{1/2}$–$1s.2p(^1P).3p\ ^2D_{3/2}$	6.6917
w	Fe XXV	$1s^2\ ^1S_0$–$1s.2p\ ^1P_1$	6.7004
J	Fe XXV	$1s.2p\ ^1P_1$–$2p^2\ ^1D_2$	6.9188
T	Fe XXV	$1s.2s\ ^1S_0$–$2s.2p\ ^1P_1$	6.9373
Lyα_2	Fe XXIV	$1s\ ^2S_{1/2}$–$2p\ ^2P_{1/2}$	6.9521
Lyα_1	Fe XXIV	$1s\ ^2S_{1/2}$–$2p\ ^2P_{3/2}$	6.9732
j_3	Fe XXIV	$1s^2.2p\ ^2P_{3/2}$–$1s.2p(^3P).3p\ ^2D_{5/2}$	7.7811
y_3	Fe XXV	$1s^2\ ^1S_0$–$1s.3p\ ^3P_1$	7.8720
w_3	Fe XXV	$1s^2\ ^1S_0$–$1s.3p\ ^1P_1$	7.8810

*Notations are from Doschek, Feldman, and Cowan (1981) for the Fe XXIII lines, Gabriel (1972) for the Fe XXIV $n = 2 \rightarrow 1$ lines, and Safronova for the Fe XXV satellite lines. We used the same notation of Heα for Heβ with a suffix "$_3$."
†Retrieved from `Chianti` v10.1.
‡Blending with weaker lines indecated by Beiersdorfer et al. (1993): *u* with Fe XXIV *v*, Fe XXIII *E8*, and Fe XXIII *E9*; *e* with Fe XXIII *E6* and Fe XXIII *E7*; *t* with Fe XXIV *m*.

the model represents both the continuum and the Ni Heα lines. In addition, we included two main lines of Fe XXV Heβ *w*, *y* (w_3, y_3 hereafter) and one satellite line of Fe XXIV j_3.

3.2.2.2 *Fitting*

We performed the fitting using the models described above for each line complex. The common settings are as follows. Each line component is represented by a Gaussian model as the Lorentz wing is invisible for the given statistics (Hitomi Collaboration 2018b). The expected width is ∼0.3 eV for *w* in the worst-case scenario, which is relatively minor. The Gaussian line widths are linked to one another. The line centers are fixed to the reference values (table 1), and the energy shift is fitted collectively. The parameters of the continuum emission component are initially fixed to those obtained in the 1.7–10 keV band fitting (sub-subsection 3.2.1), with subsequent adjustments made through renormalization for each complex. The free parameters include the normalization of each line component, as well as the energy shift and line width of each line complex.

The best-fitting model and the data are illustrated in figure 3, with the best-fitting normalization values shown in figure 4. All fits yielded satisfactory results with reduced χ^2 values of 43.07/48 for Lyα, 50.11/55 for Heα, and 46.33/58 for Heβ. The line shifts and widths are $(0.06^{+0.04}_{-0.03}, 2.4^{+0.30}_{-0.29})$ eV for Fe Heα, $(0.04^{+0.19}_{-0.04}, 3.43^{+2.12}_{-3.43})$ eV for Lyα, and $(0.1^{+0.10}_{-0.90}, 1.98^{+2.39}_{-1.98})$ eV for Heβ. The measured line shifts are consistent with one another but are small compared with the absolute uncertainty on the energy scale. For the line width of the He α complex, the systematic uncertainty is relatively small, and the measured width corresponds to 91 km s^{-1}. If the broadening is entirely attributed to thermal motion, the width implies an ion temperature of 2.1–4.8 keV.

4 Discussion

In this section, we present the line ratio diagnostics and our interpretation of the results. We start with a brief description of the physical background (subsection 4.1) and apply the diagnostics to the data (subsection 4.2).

4.1 Line ratio diagnostics

4.1.1 Physics

The upper levels of the transitions are populated through various excitation processes, but occasionally a specific process dominates. Such lines are particularly useful for line ratio diagnostics due to their straightforward dependence on plasma parameters. In collisionally ionized plasmas, two excitation

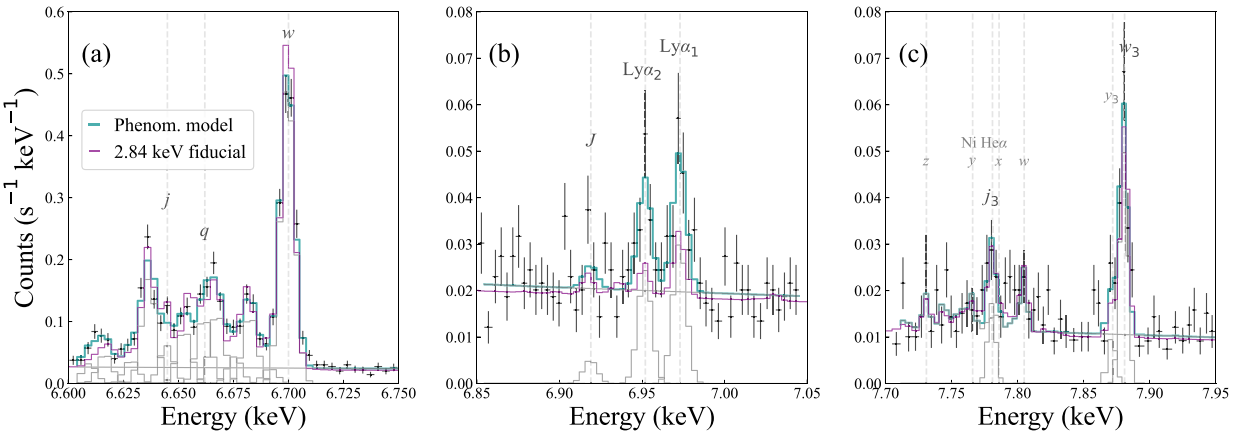

Fig. 3. Close-up views of the Resolve spectrum and the best-fitting phenomenological model for the Fe line complexes: (a) Heα, (b) Lyα, and (c) Heβ, shown in cyan. The result of the fiducial 2.84 keV thermal plasma model (figure 2) is also shown in purple. The lines used in the line ratio analysis as well as contaminated Ni Heα are annotated using the names in table 1.

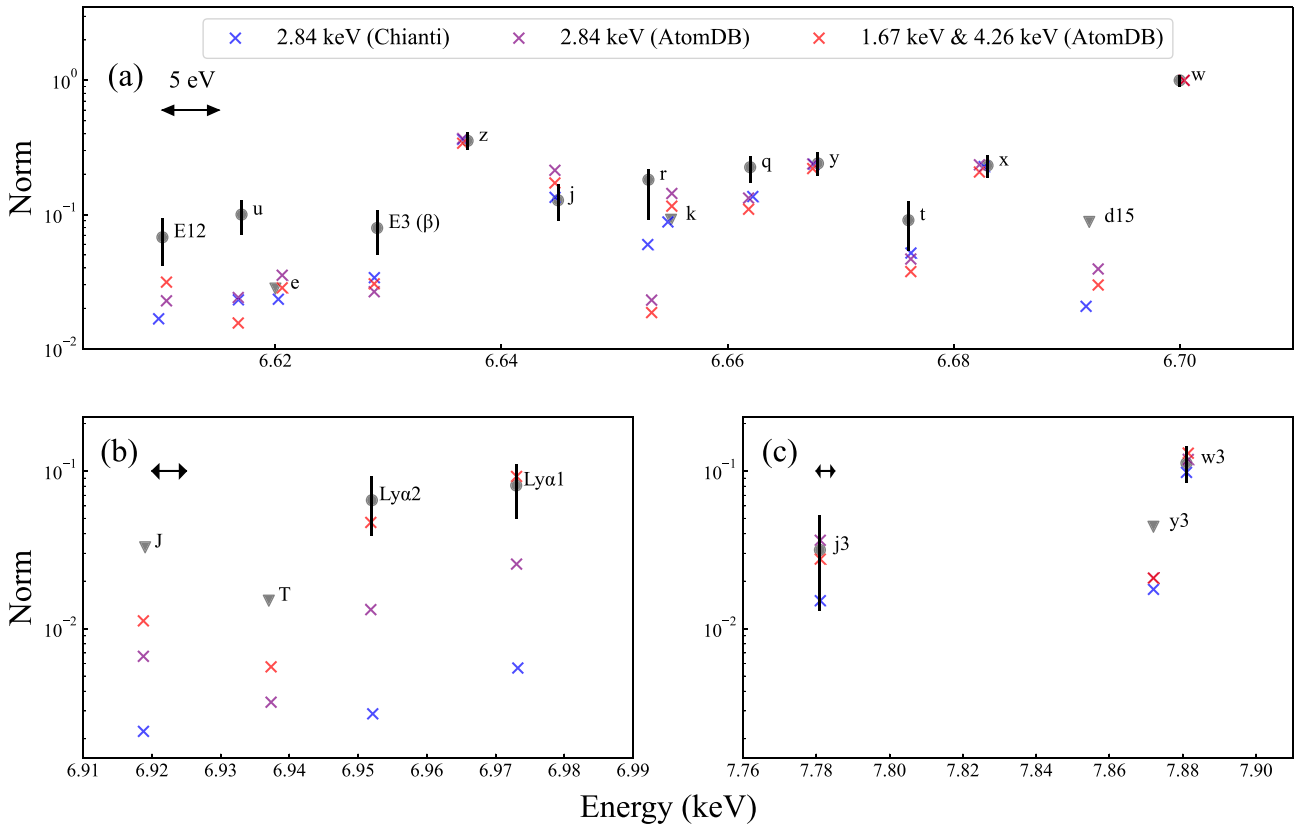

Fig. 4. Comparison of the line strengths between the observation and models for (a) Fe Heα, (b) Lyα, and (c) He β complexes. The values are normalized to Heα *w*. The data points are represented by circles with error bars if detected, or by triangles if undetected.

mechanisms play an important role (Phillips et al. 2012): direct excitation (DE) and dielectronic recombination (DR). Following previous solar observations (e.g., Watanabe 2024), we utilize their line ratios to characterize the ion charge population and the electron energy distributions, providing insights into the plasma parameters.

4.1.1.1 *Probing ion charge population*

The ratio of two DE lines from ions of adjacent charges serves as a useful measure to determine the charge population of the plasma. The DE process, also referred to as the electron impact excitation process, can be described as

$$X_i^{+m} + e(E_{\rm kin}) \rightarrow X_j^{+m,*} + e(E'_{\rm kin}) \rightarrow X_k^{+m} + h\nu(E_{jk}). \quad (1)$$

Here, a free electron transfers part of its kinetic energy $E_{\rm kin}$ to an ion, exciting the electron from the state i (mostly the ground state) to j. When they deexcite radiatively to the state k (also mostly the ground state; thus $k = i$) by emitting a photon, the DE line is formed at an energy E_{jk}. The intensity of DE lines is proportional to the amount of the ion X^{+m}. By using lines probing different m in X^{+m}, we can measure the charge population. Because the ionization and recombination rates depend sensitively on the plasma temperature, the ratio serves as a reliable diagnostic of the plasma temperature.

4.1.1.2 *Probing electron energy distribution*

For diagnosing electron energy distributions, the different formation mechanisms of DR and DE lines are leveraged. The DR process can be expressed as

$$X_i^{+m+1} + e(E_{\rm kin}) \rightarrow X_j^{+m,**} \rightarrow X_k^{+m} + h\nu(E_{jk}). \quad (2)$$

Here, when a free electron is captured by the ion X_i^{+m+1}, the released energy (comprising its initial kinetic energy $E_{\rm kin}$ and the binding energy after the capture) is used to excite a bound electron, forming a doubly excited state $X_j^{+m,**}$. This process occurs only for electrons with a specific kinetic energy that satisfies $E_{\rm kin} = -I_{\rm pot} + E_{jk}$, where $I_{\rm pot}$ is the ionization potential. As a result, the intensity of the satellite lines produced via DR reflects the electron population at this specific energy. In contrast, DE lines can be formed by any electron with kinetic energy greater than E_{jk}. This distinction makes the DR to DE line ratio a valuable probe of the electron energy distribution (Gabriel 1972; Gabriel & Phillips 1979). Figure 5 illustrates this behavior by showing the excitation energies of DE Fe XXV *w* and DR Fe XXIV *j* along with a comparison of different electron energy distributions.

For a thermal plasma, the DR to DE ratio can be expressed as a function of the temperature (see, e.g., Phillips et al. 2012):

$$\frac{I_{\rm DR}}{I_{\rm DE}} \propto \frac{\exp\left[\left(\Delta E_{\rm DE} - \Delta E_{\rm DR}\right)/kT\right]}{kT}. \quad (3)$$

The transition energies of DE and DR lines ($\Delta E_{\rm DE}$ and $\Delta E_{\rm DR}$) are usually close; thus the ratio is approximately inversely proportional to temperature, making it a useful diagnostic tool.

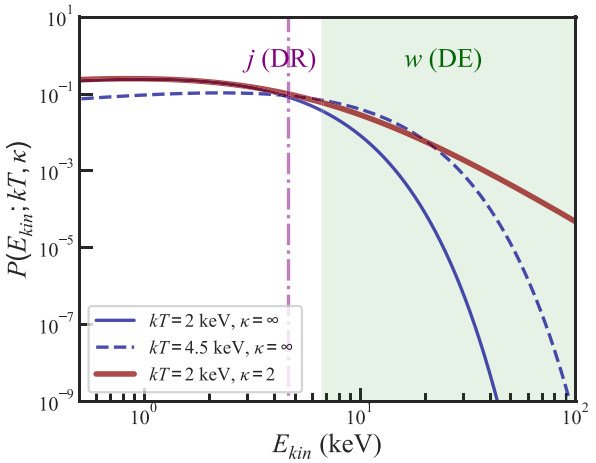

Fig. 5. Three electron energy distributions: the Maxwellian distribution with $kT = 2$ and 4.5 keV, and a κ distribution with $kT = 2$ keV and $\kappa = 2$. The κ distribution is often used to represent a distribution deviating from the Maxwellian with a power-law tail characterized by the parameter κ. It approaches the Maxwell distribution as $\kappa \to \infty$ (Oka et al. 2013). The electrons on the purple line (j) or in the green area (w) contribute to the line formation.

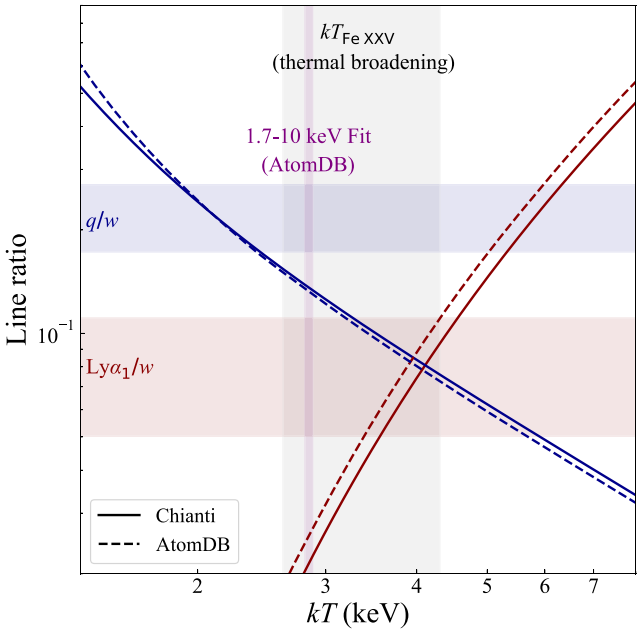

Fig. 6. Temperature diagnostics using line ratios sensitive to ion charge distribution. The line ratios of q/w (Li-like/He-like Fe) and $\mathrm{Ly}\alpha_1/w$ (H-like/He-like Fe) are shown in blue and red, respectively, for the observation (shaded areas) and calculation using `Chianti` (solid curves) and `AtomDB` (dashed curves). The best-fitting kT from the broad-band fitting using `AtomDB` (subsubsection 3.2.1) and $kT_{\mathrm{Fe\,XXV}}$ derived from the line broadening in the Heα complex are also presented.

Moreover, the ratio is highly sensitive to deviations from the Maxwellian distribution, such as the κ distribution, which exhibits an enhanced high-energy tail (figure 5). In addition to its strong dependence on the electron energy distribution, this ratio has the advantage of being independent of charge state distributions, as both lines are produced from the same parent ion.

4.1.2 Pairs in the Fe K band

We apply the diagnostics described in subsection 4.1 to the present data in the Fe K band. The strongest lines in the three complexes are Fe XXV w for Heα, Fe XXIV Lyα_1 for Lyα, and w_3 for Heβ. All of these lines originate mainly from DE processes and undergo radiative decay via an electric dipole transition to the ground state.

In the Heα complex, many satellite lines are detected (figure 3a). The Fe XXIV q line is populated primarily by inner-shell excitation from the ground state of Li-like Fe (Bely-Dubau et al. 1982). The Fe XXIV j line, on the other hand, is a DR line that reflects the population of He-like Fe (Bely-Dubau et al. 1982). Another well known DR line, Fe XXIV k (e.g., Beiersdorfer et al. 1992; Phillips et al. 2012), is significantly blended with the Fe XXIV r line in our dataset. These DR satellite lines are formed with a spectator electron in the L shell, but a similar DR process can also occur with a spectator electron in the M shell or higher. Some of these lines (e.g., the $d13$ and $d15$ lines) were included in our phenomenological fitting; however, they are blended with the Fe XXV w line, making their individual contributions difficult to isolate. In the Lyα complex (figure 3b), only upper limits were obtained for the two satellite lines Fe XXV J and T. Among them, the J line was better constrained and thus used in our analysis. In the Heβ complex (figure 3c), j_3 is the only DR line clearly detected, which corresponds to a 1s–3p equivalent of the 1s–2p transition associated with the j line in the Heα complex.

Among these lines, we used two line ratios to investigate the ion charge distribution and three line ratios to probe the electron energy distribution. The former consists of (i) Fe XXIV q/Fe XXV w and (ii) Fe XXIV Lyα_1/Fe XXV w. The latter consists of (iii) Fe XXIV j/Fe XXV w in the Heα complex, (iv) Fe XXIV j_3/Fe XXV w_3 in the Heβ complex, and (v) Fe XXV J and Fe XXIV Lyα_1 in the Lyα complex. In each case, the stronger of the two lines was used as the denominator in the ratio.

For comparison, we used two spectral synthesis codes for the thermal plasma; one is `apec`/`AtomDB` v3.0.9 (Smith et al. 2001; Foster et al. 2012) and the other is `Chianti` v10.1 (Dere et al. 1997, 2023). The former is traditionally used in astrophysical plasmas, while the latter is more common in solar plasmas. They have their own atomic databases of different origins. Their differences have been studied in many cases, including the analyses using the SXS data (Hitomi Collaboration 2018b). For some Fe K-shell lines considered here, we found that the discrepancy can be as large as a factor of two. We do not aim to determine which database is more accurate in this paper. Instead, we present their differences to highlight the need for further refinements in atomic data.

4.2 Application

4.2.1 Single-temperature plasma

4.2.1.1 Ion charge distribution

We first examined the charge distribution using q/w and Lyα_1/w ratios. The q/w ratio probes the relative charge fraction between Li-like and He-like Fe ions, while the Lyα_1/w ratio probes that between He-like and H-like Fe ions. The expected line ratios are calculated as a function of kT based on `Chianti` and `AtomDB` and compared with the observed ratios (figure 6). In this temperature range, the fraction of more highly ionized species increases monotonically, causing the q/w ratio to decrease and the Lyα_1/w ratio to increase as kT increases.

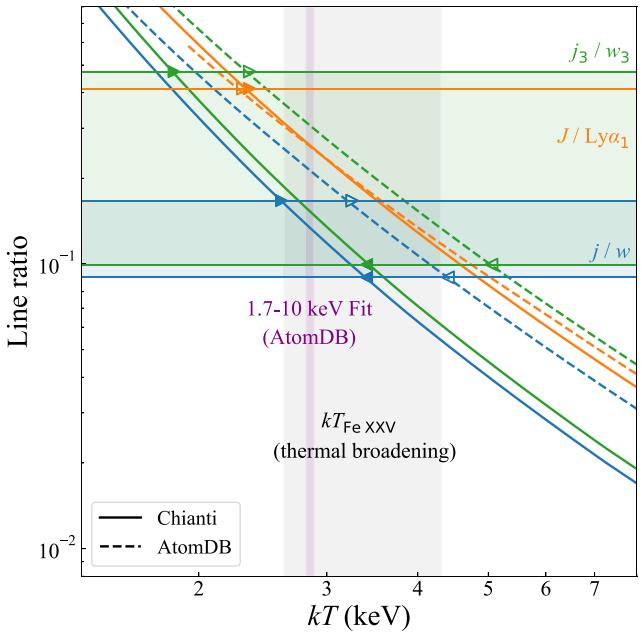

Fig. 7. Temperature diagnostics using line ratios sensitive to electron energy distribution. The line ratios of j/w, $J/\mathrm{Ly}\alpha_1$, and j_3/w_3 are shown in blue, orange, and green, respectively for the observation (shaded area and upper and lower limit lines for j/w and j_3/w_3, while only the upper limit line is shown for $J/\mathrm{Ly}\alpha_1$) and calculations using `Chianti` (solid curves) and `AtomDB` (dashed curves). The best-fitting kT from the broad-band fitting using `AtomDB` (sub-subsection 3.2.1) and $kT_{\mathrm{Fe\,XXV}}$ derived from the line broadening in the Heα complex are also presented.

The observed q/w ratio suggests $kT \sim 2$ keV, while the Lyα/w ratio indicates ~4 keV. This clearly demonstrates that a single-temperature representation is inadequate for this plasma. Indeed, fitting the broad-band spectrum with a single temperature (sub-subsection 3.2.1) resulted in a best-fitting temperature of 2.84 keV, which is inconsistent with both line ratios.

4.2.1.2 *Electron energy distribution*

We next performed diagnostics using the three DR to DE line ratios (figure 7). In this temperature range, as the plasma temperature kT increases, the population of higher-energy electrons in the electron energy distribution increases (figure 5), causing the DR/DE line ratio to decrease with increasing kT. The two databases produce different results, with `Chianti` systematically predicting smaller values for all three ratios compared to `AtomDB` at a given kT. Using `Chianti`, we found that $kT = 2.6$–3.4 keV satisfies all three ratios. Using `AtomDB`, 3.3–4.3 keV satisfies all three ratios. This is again inconsistent with the broad-band fitting result using `AtomDB` of 2.84 keV.

4.2.2 Deviations from single-temperature plasma

We found that a single-temperature representation, which worked for the broad-band fitting (sub-subsection 3.2.1), does not work for the line ratio diagnostics (sub-subsection 4.2.1). We now explore three deviations from it below.

4.2.2.1 *Multi-temperature plasma*

The simplest deviation from a single-temperature model is to introduce another single-temperature component of a different kT. We revisited the broad-band spectral fitting and applied the two-temperature plasma model. The free parameters include the abundances of major elements and the ISM absorption column (N_{H}) common between the two components, and the plasma temperature kT_i and emission measure EM_i of the two components ($i \in \{1, 2\}$). By constraining $kT_1 < 2$ keV and $kT_2 > 2$ keV, we obtained improved results over the one-temperature fitting with a reduced $\chi^2 = 2203.43/2169$. The best-fitting parameters are shown in table 2, while the model is in figure 8.

Table 2. Two-temperature thermal plasma model fitting results.

Parameters	Low-kT component		High-kT component
N_H (10^{21} cm^{-2})		$1.3^{+1.7}_{-1.3}$	
kT (keV)	$1.67^{+0.10}_{-0.14}$		$4.26^{+0.31}_{-0.30}$
EM (10^{54} cm^{-3})	$26^{+3.1}_{-3.0}$		$13^{+2.6}_{-1.9}$
Z_{Si} ($Z_\odot$)		$0.35^{+0.06}_{-0.05}$	
Z_{S} ($Z_\odot$)		$0.32^{+0.03}_{-0.03}$	
Z_{Ar} ($Z_\odot$)		$0.48^{+0.07}_{-0.06}$	
Z_{Ca} ($Z_\odot$)		$0.51^{+0.07}_{-0.07}$	
Z_{Fe} ($Z_\odot$)		$0.28^{+0.01}_{-0.01}$	
Z_{Ni} ($Z_\odot$)		$0.37^{+0.16}_{-0.16}$	

The two-temperature model is also favored when considering the Fe line ratios. In figure 4, the two-temperature model enhances the consistency between the observed and calculated line strengths, particularly for the Lyα lines. However, we still observe that the Fe XXIV q and t lines and Fe XXIII $E12$ and $E3$ lines are stronger in the observation than in the calculation, which may suggest the presence of an even lower temperature component (Doschek et al. 1981).

4.2.2.2 *Suprathermal electron distribution*

Next, instead of adding another thermal plasma component, we investigated whether modifying the electron energy distribution could explain the observed line ratios. The κ distribution is commonly used in solar coronae (e.g., Dudík & Dzifčáková 2021) to represent the distribution with a power-law suprathermal tail upon a thermal Maxwellian distribution. The parameter $\kappa \in [1.5, \infty)$ represents the relative fraction of the suprathermal population, while kT_{M} is for the main thermal population. At $\kappa \to \infty$, the distribution asymptotes to the Maxwellian distribution of a kT_{M} temperature.

Using the κ model based on `AtomDB` (Cui et al. 2019), we calculated the five line ratios as a function of κ and kT_{M} and restricted their values using the observed ratio (figure 9). No combination of κ and kT_{M} can explain all the observed ratios. Therefore, we conclude that the suprathermal electron distribution is not justified in a way that accounts for the observed line ratios.

4.2.2.3 *Non-equilibrium plasma*

We also investigated the possibility that the electron (kT_{e}) and ionization (kT_{Z}) temperatures are different in two ways: one is the ionizing plasma ($kT_{\mathrm{e}} > kT_{\mathrm{Z}}$) and the other is the recombining plasma ($kT_{\mathrm{e}} < kT_{\mathrm{Z}}$). Both scenarios are characterized by two parameters: the electron temperature kT_{e} and the Coulomb relaxation timescale $\tau \equiv \int n_{\mathrm{e}} dt$, in which n_{e} is the electron density.

The diagnostics for the ionizing and recombining plasmas are shown in figures 10 and 11, respectively. We access the NEI

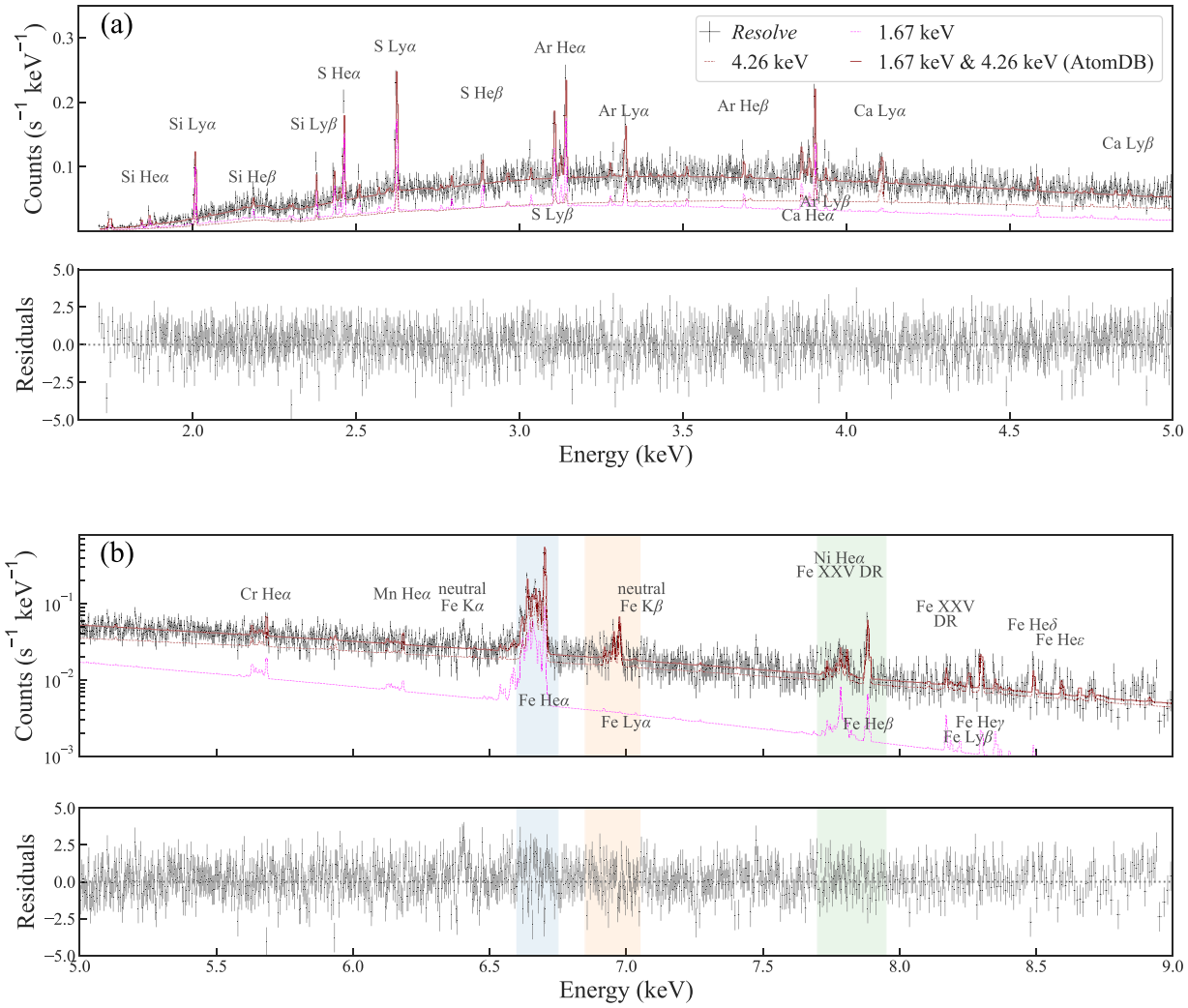

Fig. 8. Two-temperature plasma model and the residuals from the data in the (a) 1.7–5.0 and (b) 5.0–9.0 keV bands.

model based on `AtomDB` via the `PyAtomDB` interface (Foster & Heuer 2020) to calculate the line ratios. For the ionizing plasma, all ions start with neutral states at $\tau = 0$. For the recombining plasma, all ions start in the fully ionized state at $\tau = 0$. Both kT_e and n_e are assumed to remain constant. In both cases, no parameter space was found that satisfies all five line ratio constraints, suggesting that these models are not likely solutions. It is reasonable that the plasma reaches some equilibrium, particularly for the stellar coronae at quiescence like the one presented here.

5 Conclusion

With the unprecedented spectral resolution of XRISM Resolve, detailed spectra for Fe K-shell lines were obtained for the stellar corona from GT Mus at its quiescent state. The satellite lines of Fe XXIV–XXIV, including those in the Fe Heβ complex, have become accessible for the first time for stellar sources other than the Sun.

We performed a phenomenological model fitting for the lines in three line complexes. Two pairs of DE and three pairs of DR/DE lines were used for the line ratio analysis: q/w, Lyα_1/w, j/w, J/Lyα1, and j_3/w_3. The lines in each pair have close central energies, providing robust diagnostic results against uncertainties in the effective area across the broad energy band. The temperature diagnostics through the ion charge population and the electron energy distribution revealed that a single-temperature plasma description is insufficient, requiring deviation from it. We investigated the two-temperature and κ distributions and the ionizing or recombining plasmas, and found that the two-temperature (1.7 and 4.3 keV) solution is preferred, which is also consistent with the broad-band fitting in the 1.7–10 keV and the thermal broadening of the Fe XXV Heα complex.

This study demonstrates the capability of X-ray microcalorimeter spectra to diagnose plasmas in celestial stellar sources. The same technique is applicable to spectra during flares, which may reveal interesting non-equilibrium pheonomena. Even for the Sun, there are only limited results in EUV (Kawate et al. 2016; Dzifčáková et al. 2018) and X-rays (Doschek & Tanaka 1987) for such features. Many celestial stellar sources are known to exhibit gigantic and long-lasting flares compared to the Sun (Tsuboi et al. 2016), and their observations with Resolve are awaited.

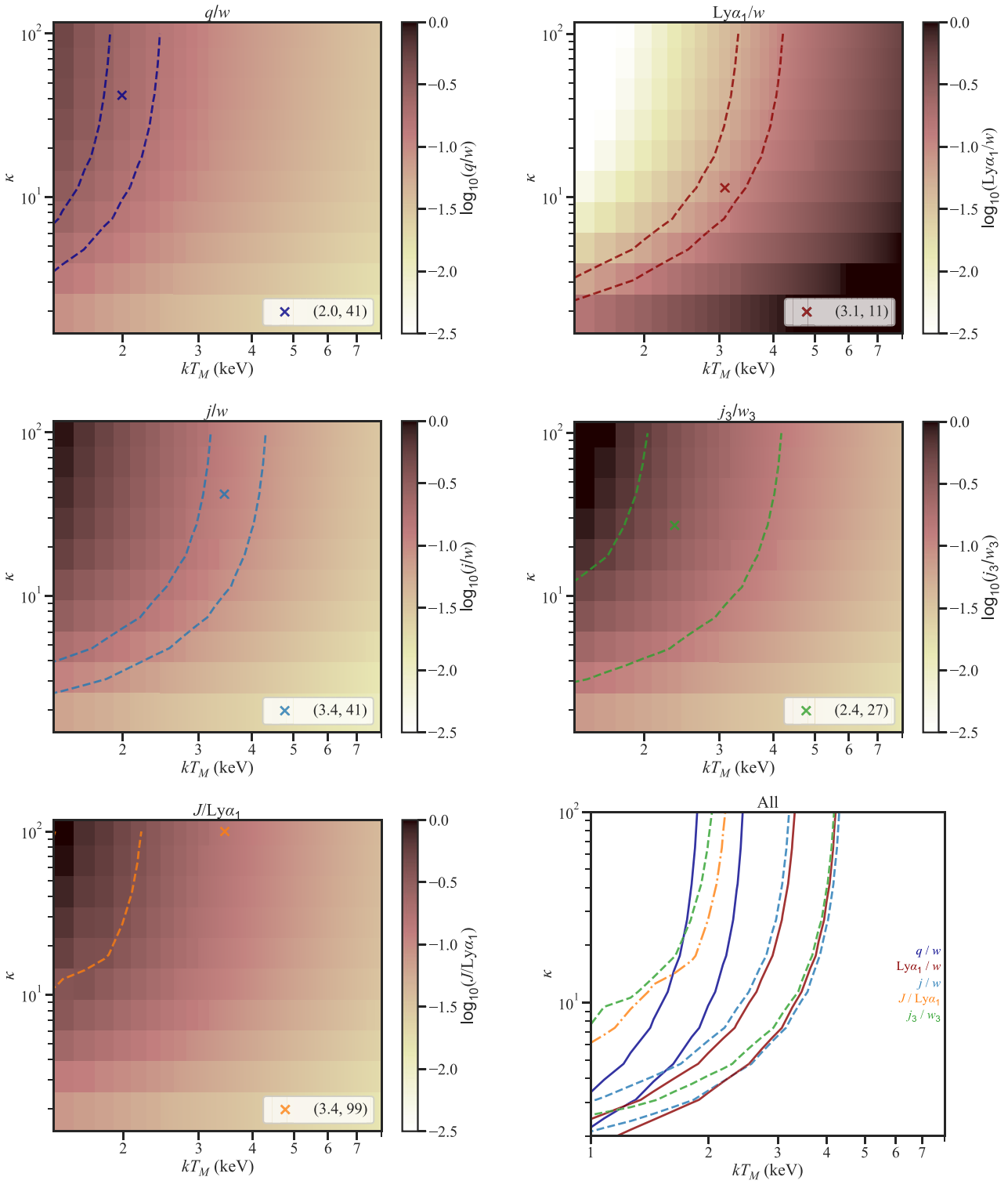

Fig. 9. Diagnostics for the κ electron energy distribution. Heatmaps are created for five line ratios based on the `AtomDB` model (Cui et al. 2019), covering the two parameters κ and $kT_{\rm M}$. The best-fitting values of the two parameters are marked with a cross, and the 90% uncertainty range is indicated with contours. Only the upper limit is provided for the J/Lyα1 ratio. All contours are assembled in the bottom right. The contour line style distinguishes the two pairs for ion charge distribution (solid lines) and three pairs for electron energy distribution (dashed lines). No space satisfies all the contours simultaneously.

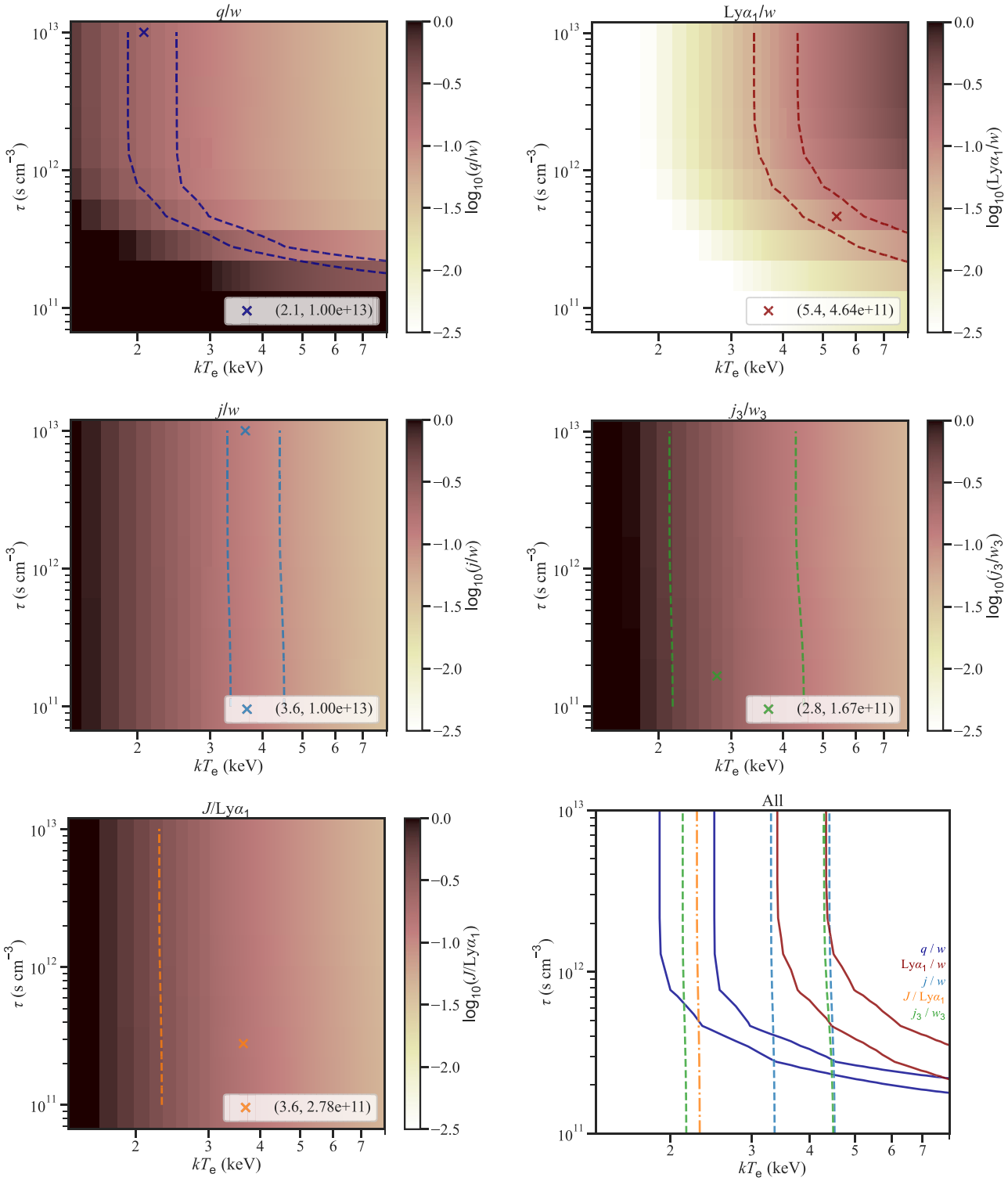

Fig. 10. Diagnostics for the ionizing plasma. The format and symbols follow figure 9. The ionizing plasma model in `AtomDB` is retrieved via `PyAtomDB` (Foster & Heuer 2020) to calculate the five line ratios as functions of the relaxation parameter τ and the electron temperature kT_e. The initial condition at $\tau = 0$ assumes that all Fe ions are neutral and the electrons have a temperature of kT_e. No space satisfies all the contours simultaneously.

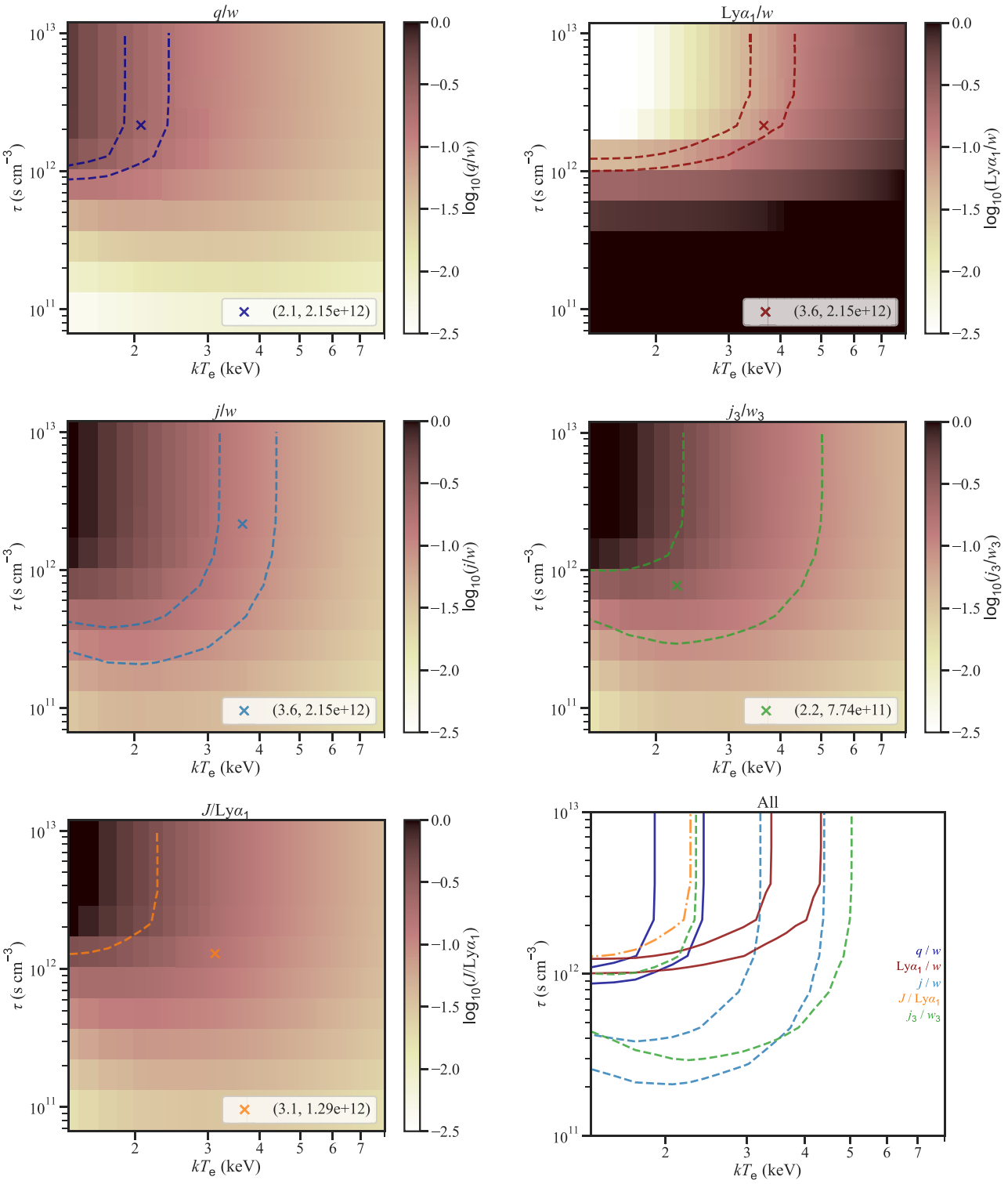

Fig. 11. Diagnostics for the recombining plasma. The format and symbols follow figure 9. The ionizing plasma model in `AtomDB` is retrieved via `PyAtomDB` (Foster & Heuer 2020) to calculate the five line ratios as functions of the relaxation parameter τ and the electron temperature kT_e. The initial condition at $\tau = 0$ assumes that all Fe ions are fully ionized and the electrons have a temperature of kT_e. No space satisfies all the contours simultaneously.

Acknowledgments

We appreciate the insightful discussions on high-resolution X-ray spectroscopy with Tetsuya Watanabe at NAOJ.We appreciate the support of Wataru Iwakiri and Yoshiaki Kanemaru in the pre-observation planning. This research has made use of data and/or software provided by the High Energy Astrophysics Science Archive Research Center (HEASARC), which is a service of the Astrophysics Science Division at NASA/GSFC. `Chianti` is a collaborative project involving George Mason University, the University of Michigan

(USA), University of Cambridge (UK), and NASA Goddard Space Flight Center (USA). This research was supported by a Grant of Joint Research by the National Institutes of Natural Sciences (NINS) (NINS program No. OML032402). The material is based upon work supported by NASA under award number 80GSFC21M0002. EB acknowledges support from NASA grants 80NSSC20K0733, 80NSSC24K1148, and 80NSSC24K1774. Part of this work was performed under the auspices of the US Department of Energy by Lawrence Livermore National Laboratory under Contract DE-AC52-07NA27344.

References

Anders, E., & Grevesse, N. 1989, Geochim. Cosmochim. Acta, 53, 197
Arnaud, K. A. 1996, ASP Conf. Ser., 101, 17
Audard, M. 2003, Adv. Space Res., 32, 927
Audard, M., Güdel, M., Sres, A., Raassen, A. J. J., & Mewe, R. 2003, A&A, 398, 1137
Beiersdorfer, P., Phillips, T. W., Wong, K. L., Marrs, R. E., & Vogel, D. A. 1992, Phys. Rev. A, 46, 3812
Beiersdorfer, P., Phillips, T., Jacobs, V. L., Hill, K. W., Bitter, M., von Goeler, S., & Kahn, S. M. 1993, ApJ, 409, 846
Bely-Dubau, F., Faucher, P., Dubau, J., & Gabriel, A. H. 1982, MNRAS, 198, 239
Collier, A. C., Haynes, R. F., Slee, O. B., Wright, A. E., & Hillier, D. J. 1982, MNRAS, 200, 869
Cui, X., Foster, A. R., Yuasa, T., & Smith, R. K. 2019, ApJ, 887, 182
Decaux, V., Beiersdorfer, P., Kahn, S. M., & Jacobs, V. L. 1997, ApJ, 482, 1076
Dere, K. P., Del Zanna, G., Young, P. R., & Landi, E. 2023, ApJS, 268, 52
Dere, K. P., Landi, E., Mason, H. E., Monsignori Fossi, B. C., & Young, P. R. 1997, A&AS, 125, 149
Doschek, G. A., Feldman, U., & Cowan, R. D. 1981, ApJ, 245, 315
Doschek, G. A., Feldman, U., Kreplin, R. W., & Cohen, L. 1980, ApJ, 239, 725
Doschek, G. A., Kreplin, R. W., & Feldman, U. 1979, ApJ, 233, L157
Doschek, G. A., & Tanaka, K. 1987, ApJ, 323, 799
Doyle, T. F., et al. 2022, Proc. SPIE, 12181, 1218160
Dubau, J., Loulergue, M., Gabriel, A. H., Steenman-Clark, L., & Volonte, S. 1981, MNRAS, 195, 705
Dudík, J., & Dzifčáková, E. 2021, in Kappa Distributions: From Observational Evidences via Controversial Predictions to a Consistent Theory of Nonequilibrium Plasmas, ed. M. Lazar & H. Fichtner (Cham: Springer), 53
Dzifčáková, E., Zemanová, A., Dudík, J., & Mackovjak, Š. 2018, ApJ, 853, 158
Eckart, M. E., et al. 2024, Proc. SPIE, 13093, 130931P
Eze, A. C., Esaenwi, S., & Madu, F. O. 2022, Adv. Space Res., 69, 499
Feldman, U., Doschek, G. A., Kreplin, R. W., & Mariska, J. T. 1980, ApJ, 241, 1175
Foster, A. R., & Heuer, K. 2020, Atoms, 8, 49
Foster, A. R., Ji, L., Smith, R. K., & Brickhouse, N. S. 2012, ApJ, 756, 128
Gabriel, A. H. 1972, MNRAS, 160, 99
Gabriel, A. H., & Paget, T. M. 1972, J. Phys. B, 5, 673
Gabriel, A. H., & Phillips, K. J. H. 1979, MNRAS, 189, 319
Gaia Collaboration 2016, A&A, 595, A1
Gaia Collaboration 2023, A&A, 674, A1
Gendreau, K. C., et al. 2016, Proc. SPIE, 9905, 99051H
Gu, M. F., Beiersdorfer, P., Brown, G. V., Graf, A., Kelley, R. L., Kilbourne, C. A., Porter, F. S., & Kahn, S. M. 2012, Canadian J. Phys., 90, 351
Hell, N., et al. 2020, X-Ray Spectrometry, 49, 218
Hitomi Collaboration 2018a, PASJ, 70, 9
Hitomi Collaboration 2018b, PASJ, 70, 12
Huenemoerder, D. P., Phillips, K. J. H., Sylwester, J., & Sylwester, B. 2013, ApJ, 768, 135
Ishisaki, Y., et al. 2022, Proc. SPIE, 12181, 121811S
Kaastra, J. S., & Bleeker, J. A. M. 2016, A&A, 587, A151
Kawate, T., Keenan, F. P., & Jess, D. B. 2016, ApJ, 826, 3
Kelley, R. L., et al. 2016, Proc. SPIE, 9905, 99050V
Kilbourne, C. A., et al. 2018a, J. Astron. Telesc. Instrum. Syst., 4, 011214
Kilbourne, C. A., et al. 2018b, PASJ, 70, 18
Koyama, K., et al. 2007, PASJ, 59, 23
Lebrun, F., et al. 2003, A&A, 411, L141
Maksimovic, M., Pierrard, V., & Riley, P. 1997, Geophys. Res. Lett., 24, 1151
Matsuoka, M., et al. 2009, PASJ, 61, 999
McCammon, D., Moseley, S. H., Mather, J. C., & Mushotzky, R. F. 1984, J. Applied Phys., 56, 1263
Midooka, T., Tsujimoto, M., Kitamoto, S., Nakaniwa, N., Maeda, Y., Ishida, M., Ebisawa, K., & Tominaga, M. 2021, J. Astron. Telesc. Instrum. Syst., 7, 028005
Mihara, T., et al. 2011, PASJ, 63, S623
Mitsuda, K., et al. 2007, PASJ, 59, S1
Mizumoto, M., et al. 2025, J. Astron. Telesc. Instrum. Syst., 11, 042005
Mochizuki, Y., et al. 2025, J. Astron. Telesc. Instrum. Syst., 11, 042002
Mori, K., et al. 2022, Proc. SPIE, 12181, 121811T
Murdoch, K. A., Hearnshaw, J. B., Kilmartin, P. M., & Gilmore, A. C. 1995, MNRAS, 276, 836
Noda, H., et al. 2025, PASJ, 77, S10
Nordon, R., & Behar, E. 2007, A&A, 464, 309
Oka, M., Ishikawa, S., Saint-Hilaire, P., Krucker, S., & Lin, R. P. 2013, ApJ, 764, 6
Pandey, J. C., & Singh, K. P. 2012, MNRAS, 419, 1219
Parmar, A. N., Culhane, J. L., Rapley, C. G., Antonucci, E., Gabriel, A. H., & Loulergue, M. 1981, MNRAS, 197, 29P
Phillips, K. J. H., Feldman, U., & Landi, E. 2012, Ultraviolet and X-ray Spectroscopy of the Solar Atmosphere (Cambridge: Cambridge University Press)
Porter, F. S., et al. 2016, J. Low Temperature Phys., 184, 498
Porter, F. S., et al. 2024, Proc. SPIE, 13093, 130931K
Sanz-Forcada, J., Brickhouse, N. S., & Dupree, A. K. 2002, ApJ, 570, 799
Sasaki, R., et al. 2021, ApJ, 910, 25
Sguera, V., Sidoli, L., Paizis, A., & Bird, A. J. 2016, MNRAS, 463, 2885
Shirron, P. J., et al. 2018, J. Astron. Telesc. Instrum. Syst., 4, 021403
Smith, R. K., Brickhouse, N. S., Liedahl, D. A., & Raymond, J. C. 2001, ApJ, 556, L91
Smith, R. K., & Hughes, J. P. 2010, ApJ, 718, 583
Takahashi, T., et al. 2018, J. Astron. Telesc. Instrum. Syst., 4, 021402
Tanaka, K. 1986, PASJ, 38, 225
Tanaka, K., Watanabe, T., Nishi, K., & Akita, K. 1982, ApJ, 254, L59
Tashiro, M., et al. 2020, Proc. SPIE, 11444, 1144422
Tsuboi, Y., et al. 2016, PASJ, 68, 90
Vink, J. 2020, Physics and Evolution of Supernova Remnants (Cham: Springer)
Watanabe, T. 2024, ApJ, 965, 41
Wilms, J., Allen, A., & McCray, R. 2000, ApJ, 542, 914
Winkler, C., et al. 2003, A&A, 411, L1
XRISM Collaboration 2024, PASJ, 76, 1186
XRISM Collaboration 2025a, ApJ, 982, L5
XRISM Collaboration 2025b, Nature, 638, 365
XRISM Collaboration 2025c, PASJ, 77, L1
Xu, X.-j., Wang, Q. D., & Li, X.-D. 2016, ApJ, 818, 136
Yamaguchi, H., & Ohshiro, Y. 2022, in Handbook of X-ray and Gamma-ray Astrophysics, ed. C. Bambi & A. Sangangelo (Singapore: Springer), 99

Received: 2025 March 9; Accepted: 2025 April 9